Oxidation of Thin Nickel-Based Superalloy Specimens: Kinetics Study and Mechanical Integrity

Charles Romain, Damien Texier, Clara Desgranges, Jonathan Cormier, Stéphane Knittel, Daniel Monceau, Denis Delagnes

Oxidation of Thin Nickel-Based Superalloy Specimens: Kinetics Study and Mechanical Integrity

Charles Romain[1] · Damien Texier[1] · Clara Desgranges[2] · Jonathan Cormier[3] · Stéphane Knittel[4] · Daniel Monceau[5] · Denis Delagnes[1]

Abstract
The oxidation behavior of a nickel-based superalloy was investigated from 650 to 1,000 °C for up to 1,000 h in air. Samples with thicknesses ranging from 20 to 500 µm were used to document the evolutions of microstructure and oxide scale. Oxidation products and subsurface evolution of the metal microstructure were characterized by XRD and EDS analyses. Local breakaway was observed after 600 h at 800 °C and after 100 h at 900 °C due to the full consumption of Cr from the alloy. Room temperature tensile tests were performed on aged and pre-oxidized specimens with thicknesses ranging from 20 µm to 500 µm, at 800 °C. The results were compared to tensile tests performed on the as-received metallurgical state. Both size effects due to sample thickness reduction and to sample thickness/pre-oxidation width ratio were examined onto the mechanical behavior. Interestingly, the formation of TCP phases, the oxide layer and the subsequent Cr-depleted subsurface region from either aging or oxidation treatments impairs the mechanical integrity. Bulk and subsurface regions are impacted, especially for tens-of-micrometer thin samples.

Keywords Nickel-based superalloys · High-temperature oxidation · Breakaway · Gradient of microstructure and properties · Microtensile testing

Introduction

Nickel-based superalloys are used as structural components of several generations of aircraft engines. The reduction in fuel consumption, for both environmental and economic matters, involves the manufacturers to design engines that can

✉ Charles Romain
charles.romain@mines-albi.fr

withstand ever-higher operating temperatures. The temperature range for turbine disk during the engine cycle is usually low enough for high-temperature oxidation not to be considered as a critical design criteria. Therefore, disk alloys do not require any additional protections (coatings, air cooling, etc.). Nevertheless, temperature tends to increase in turbines, and parts are also designed thinner for mass reduction, so that surface reactivity has to be now taken into account [1].

High-temperature oxidation alters both the surface and the subsurface region of the materials, leading to the formation of outer and inner oxidation products, metal recession but also a gradient in chemical composition, microstructure and physical properties [2]. Evaluating and predicting the environment-assisted microstructure evolutions due to surface reactivity to further model the local deformation/damage evolution within the material is a challenging issue for engine manufacturers [3, 4]. Therefore, the high-temperature oxidation behavior of a chromia-forming polycrystalline nickel-based superalloy was examined in the present study using ultrathin specimens. This was done to investigate the changes in the type of oxides being formed, i.e., the breakaway oxidation due to Cr depletion [5]. The influence of the surface reactivity on the tensile properties of thin microtensile specimens is to be addressed [6]. Scaling approach using ultrathin specimens aims to echo the long-term exposure conditions needed to activate breakaway on conventional size specimens for very short exposures times, thanks to the limited amount of alloying elements [7–9].

The use of thin samples for oxidation and for mechanical testing results from the desire to exacerbate the effect of the oxidation-affected region up to breakaway phenomenon activation on the mechanical integrity. However, size reduction in mechanical samples to dimensions comparable with the microstructure scale could arise with technical and scientific issues. For a sample to be representative of the materials mechanical behavior, the threshold is set as the representative volume element (RVE) with a sufficient size to provide an appropriate homogenized behavior. This point leads to investigate the number of grains contained in the sample's thickness for a given polycrystalline material. The activation of breakaway mechanisms for reasonable oxidation durations requires samples as thin as technologically possible. A 20-μm-thin sample provides a 0.04-mm^2 section with 1 to 3 grains in thickness for an ASTM 10 grain-sized alloy but hundreds of thousands of grains in the 2-mm-wide and 5-mm-long gage region. As RVE is questionable in the section of samples and animates the scientific community disagreements on the use of micromechanics, the gage volume of the thinnest sample fulfills RVE requirements in terms of materials considerations and elastic behavior; the Young's modulus was found constant and independent of the sample thickness on all tensile tests. Disparities in the plastic behavior between surface grains and core grains might come from the presence of free surface compared to grain boundaries. A change in mechanical behavior is supposed from polycrystalline behavior to multicrystalline behavior for thin samples as demonstrated by Texier et al. on Inconel 718 and Keller et al. on pure nickel [7, 10]. The transition of behavior is expected between 30 and 60 μm according to the average grain size of ASTM of 8–9.

The present paper intends to explore the microstructure evolutions and oxidation kinetics up to the breakaway using ultrathin samples. Their consequences onto the mechanical properties and lifespan of materials are also exposed. The experimental results were obtained after oxidation holding times up to 1,000 h between 650 and 1,000 °C for samples of different thicknesses ranging from 500 µm down to 20 µm with t/d ratio (thickness/grain size) of 2 to 50.

Experimental Procedures

The material used in the present study was a γ/γ' polycrystalline nickel-based superalloy with a grain size index of 8–9 (ASTM), i.e., 5–15 µm, and a typical composition presented in Table 1. The samples for oxidation test with a 10×15 mm size were taken from a forged piece via electrical discharge machining and further drilled (Ø 1.5 mm) for holding during oxidation tests. Samples with thicknesses ranging from 15 to 500 µm with thickness deviations less than 2 µm were obtained by mechanical polishing using a precision polishing jig following the method detailed in previous work by Texier et al. [11]. The samples were ground then polished using the jig on SiC paper down to a P2400/800 grit with sufficient material removal for each SiC paper to minimize residual stresses at the surface of the samples and produce a repeatable surface finishing. All sides were manually polished to the same surface finish prior to grinding. The final dimensions (after polishing, primary ultrasonic ethanol and drying cleaning) were measured via optical analysis using a LEICA DMS 300 calibrated microscope for length and width to allow surface computation through edge detection algorithms (OpenCV python library [12]). Thickness was measured via a 1 µm precision micrometer on a 5-point grid. Specimens were finally cleaned following a sequence constituted by: ultrasonic acetone immersion (10 min), drying, ultrasonic ethanol (20 min) and final drying, followed by the initial mass measurement. Isothermal oxidation was performed in static laboratory air using a Nabertherm furnace. Oxidation samples were suspended using platinum wires during oxidation tests at 650, 700, 800, 900 and 1,000 °C. For each temperature, different holding times were investigated: 10, 30, 100, 200, 600 and 1,000 h. Samples were introduced in the hot furnace and air-quenched after oxidation interruption. The temperature was controlled via two K-type thermocouples positioned at different locations inside the furnace, one being in contact with the samples.

Mass gain measurements were evaluated using a Sartorius MC5 with 2 µg accuracy.

X-ray diffraction (XRD) analyses were carried out using a X'PERT-PANALYTICAL from PHILIPS with a Cu-Kα radiation (λ = 1.54 Å), covering a range of angles (2θ) from 15° to 100° with a step size of 0.033°.

Table 1 Nominal composition of the studied nickel-based superalloy (wt %)

Ni	Cr	Co	Al	Ti	Fe
Bal	15 ± 2%	13.5 ± 2%	2 ± 0.5%	4 ± 1%	1 ± 0.5%

Cross-sectional (supported by metallic rings in cold resin) and surface observations were performed using a field-emission gun scanning electron microscope (FEG-SEM) Nova NanoSEM 450 from THERMOFISHER SCIENTIFIC in a backscattered electron mode to document the oxide scale and the in-depth microstructure evolution of the alloy. Chemical analyses using energy-dispersive X-ray spectroscopy (EDS) were conducted using a FEG-SEM JEOL JSM 7800F Prime equipped with an EDS SDD X-Max 80 mm^2 detector from Oxford Instruments to characterize the depletion profile and progressive consumption of elements involved in the oxidation reactions. Mass gain measurements together with XRD and micrograph observations enabled the characterization of the oxide scale, the oxidation kinetics as well as the microstructural evolutions up to potential breakaway phenomenon.

For the mechanical tests, three different metallurgical states were investigated: (1) as-received state, corresponding to pre-machining ring-rolled material, (2) "aged" state, corresponding to samples with ground surfaces after heat treatment to remove the surface/subsurface-affected layer (oxidized or depleted in Cr) and (3) "oxidized" state, corresponding to ground samples before heat treatment to investigate the surface/subsurface-affected layer effects. Mechanical tests were performed using specimens of 500 µm, 100 µm, 50 µm and 20 µm thicknesses for the three metallurgical states. Thicknesses of 250, 75 and 35 µm were added for as-received state to better characterize the effect of sample thickness onto the mechanical response. Tensile tests were conducted using an electromechanical INSTRON tensile machine equipped with a SCAIME 500 N load cell for samples thicknesses below 150 µm and 5 kN load cell for thicker samples with constant cross-head displacement rate. Elongation measurement of the gage area was assessed using contactless extensometry using digital image correlation techniques. A black speckle was sprayed onto a white background at the samples surface and was optically tracked synchronously to the room temperature tension tests. Displacement/deformation was computed using VIC digital image correlation (DIC) algorithm [13].

Oxidation Behavior

The mass changes recorded for the 500-µm-thick samples for all oxidation durations are reported in Fig. 1a. A secondary y-axis is used to plot the mass gain in this large temperature window (left y-axis for 650 °C to 800 °C and secondary right y-axis for 900 °C and 1000 °C). The oxidation behavior reported in Fig. 1a follows a parabolic law in agreement with the Wagner's theory [14]. Experimental mass gain data are presented in Fig. 1a, alongside the associated oxidation parabolic rate constant k_p value for each temperature on the upright corner. The oxidation kinetics are in agreement with those of similar alloys (see Fig. 11 in [15]). Figure 1b models the time to full Cr consumption expected for sample thicknesses in range 20–500 µm. The dots represent experimental points, and the lines model the couple thickness/time for the studied temperatures according to Eq. (1). Experimental points located above the model lines are supposed to reach breakaway, with experimental confirmation of breakaway presence with full dots.

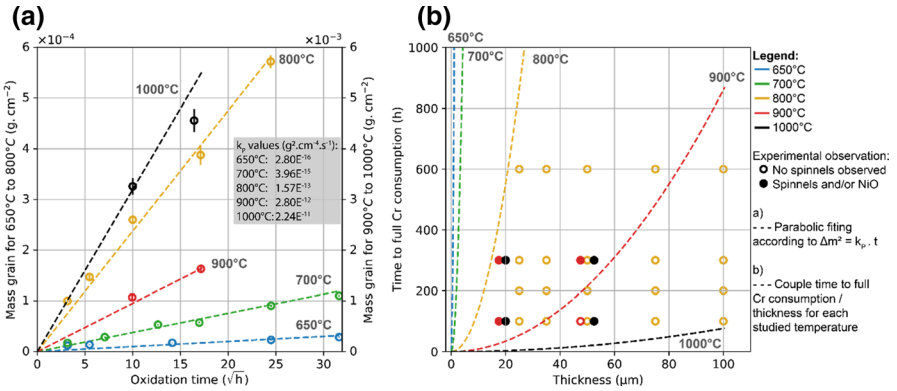

Fig. 1 **a** Mass grain (650 °C to 800 °C on the left y-axis, 900 °C to 1000 °C on the right y-axis) versus time and parabolic rate constant for 500-µm-thick samples, **b** time to full Cr consumption as function of the thicknesses for different temperatures ranging from 650 °C to 1000 °C

$$t = \left(\frac{1}{k_P}\right) \cdot \left(\frac{3 \cdot M_O \cdot \rho \cdot W_{Cr} \cdot e}{4 \cdot M_{Cr}}\right)^2 \tag{1}$$

where t stands for time to full Cr consumption (hours), k_P is the parabolic constant ($g.cm^{-2}$), Mi the molar mass of the i element ($g.mol^{-1}$), ρ the density of the alloy ($g.cm^{-3}$), W_i the weight percent of the i element (wt %) and e the thickness of the sample (cm).

With Eq. (1), it is assumed that chromium is the only chemical element being oxidized ($Cr + \frac{3}{4}O_2 = \frac{1}{2}Cr_2O_3$). Equation (1) is based on a simple mass balance between the oxygen uptake to form chromia oxide layer with parabolic kinetics and the total amount of chromium available in the material. This equation is a simple form of Eq. 20 in ref. [9], for a full depletion of Cr neglecting the diffusion of Cr in the alloy. Hence, it leads to an overestimation of the time to breakaway. It is then used as a first approximation.

Bulk specimens, *i.e.,* non-limited materials, developed an outer and continuous Cr_2O_3 layer topped with sparsely distributed TiO_2 rutile. Internal oxidation with formation of alumina Al_2O_3 oxide for all the exposure times is also evidenced for every test performed at 800, 900 and 1000 °C (see Fig. 2). Chen et al. reported similar oxidation products in suchlike alloys [16]. No spallation was observed after heat treatment up to 1000 °C. External surface oxidation evolves with the samples thickness, oxidation duration and temperature increase, leading to the formation of fast-growing oxides, *i.e.,* spinels and NiO, also known as local breakaway phenomenon. The activation energy for the oxidation temperature range 650–1000 °C is $Ea = 314 kJ.mol^{-1}$.

Some cross-sectional SEM analysis of oxidized 20-µm-thick samples is presented in Fig. 2, in the case of oxidation tests performed at 800 °C for 600 h (Fig. 2 a) and at 900 °C for 100 h (Fig. 2 b). XRD and EDS analyses confirmed the formation of oxides similar to the ones formed on thicker samples observed in Fig. 2 a). Fast-growing oxides $CoCr_2O_4$ (containing also Fe, Ni instead of Co)

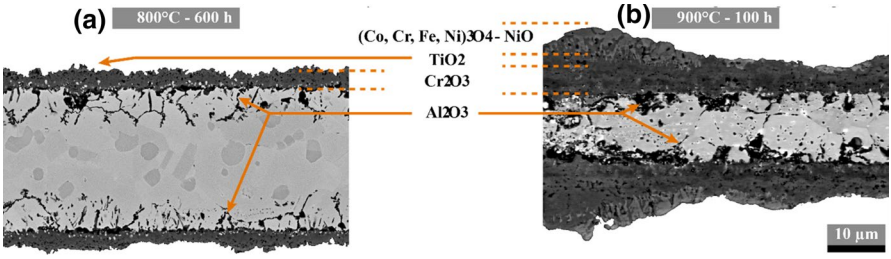

Fig. 2 SEM BSE cross-sectional observation of initial 20-µm-thick samples oxidized at **a** 800 °C during 600 h and **b** 900 °C during 100 h

alongside *NiO* formation above the external chromia layer are also evidenced via XRD and in (Fig. 2b and Fig. 3e). Thébaut, Németh and Chateau drove the same conclusions studying the oxidation kinetics of AD730™ and Udimet 720Li, which are similar to the present material in terms of chemical composition, microstructure and processing method [17–19].

Ultrathin samples, *i.e.,* volume-limited samples, demonstrate equivalent oxide growth kinetics for shorter times compared to thick samples until a threshold time for which the bulk (i.e., core) Cr concentration decreases (illustrated in Table 2). This results in the Cr concentration to drop at the oxide/metal interface. With regard to the depletion profile, the decrease of Cr content (i.e., Cr activity) enables other elements to oxidize forming faster growing oxides.

Microstructural Evolutions due to Aging and Oxidation

High-temperature exposure alters the microstructure of the studied material due to the effects of both aging and oxidation. First, topologically closed packed (TCP) µ phases alongside borides were found to form at 800 °C within the core of bulk samples for durations longer than 200 h. This microstructure evolution is illustrated in Fig. 3 b for a 500-µm-thick sample (white particles preferentially located at grain boundaries and primary precipitates). The formation of TCP phases is also evidenced at 700 °C for 4,000 h. The time-transformation-temperature (TTT) diagram

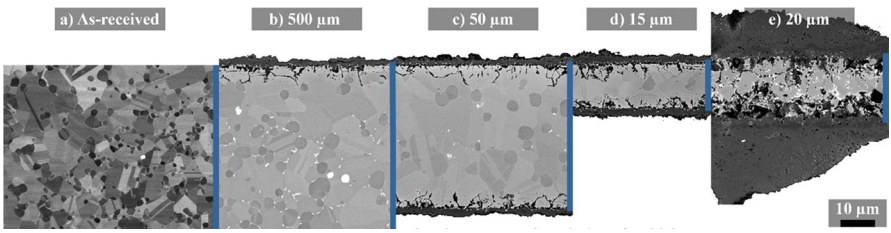

Fig. 3 **a** As-received bulk material BSE micrograph. **b**, **c**, **d** Microstructural evolutions for thicknesses 500, 50 and 15 µm observed in cross section after oxidation at 800 °C for 300 h. **e** Breakaway example on 20-µm-thick sample after 300 h at 900 °C. The blue line represents the initial thickness of the samples, prior to oxidation

Table 2 Characteristic oxide and oxidation-affected layers depths for 500-**µm**-thick samples. Bulk Cr concentration of 20-µm-thick samples on the right column

Temp (°C)	Time (h)	External oxide thickness (µm)	Internal oxide depth (µm)	Precipitates depletion depth (µm)	Cr depletion depth—EDS (µm)	TCP depletion depth (µm)	20-µm samples—Cr bulk concentration (w%)
800	300	2.4 ± 0.5	3.2 ± 1.0	5.8 ± 2.2	8.0 ± 1.0	17.1 ± 7.8	10.0 ± 1.0
900	100	5.6 ± 3.0	8.2 ± 4.9	13.0 ± 1.2	20.0 ± 2.0	–	1.5 ± 0.5
900	300	8.5 ± 3.8	14.8 ± 6.4	19.6 ± 3.9	30.0 ± 5.0	–	0.5 ± 0.5

built for Rene 65 by Wessman exhibits such metallurgical changes for such time/temperature pairs [20], also experimentally confirmed by Laurence [21, 22]. Aging also impairs the γ/γ' precipitation state in this temperature window, but this effect was not quantitatively investigated in the present study.

Oxidation leads to subsurface microstructural modifications, as shown in Fig. 3. The depleted Cr layer grew with the exposure time and temperature due to the formation of the external Cr_2O_3 layer. The oxide formation is accompanied by the extension of a subsurface primary- and secondary-precipitates-depleted layer, as reported in ref [23]. Surface reactivity also led to an internal oxide at grain boundaries. In this affected region, the alloy is depleted from both the primary, secondary and tertiary γ' and of the TCP.

Depletion and oxide thicknesses were quantitatively analyzed using images of cross-sectional BSE and EDS observations. The edge detection method of elements and linear regression between elements in case of discontinuities were used to assess both the thickness of the depleted layers and oxide scales. The results are reported in Table 2 for oxidation conditions 800 °C – 300 h, 900 °C – 100 h and 300 h. Similar extension of the oxidation-affected subsurface region and oxide scales was found regardless of the sample thickness for 300 h at 800 °C, i.e., as long as breakaway condition is not met (Fig. 3). The disparities in external oxide thickness at 900 °C result from local breakaway phenomena associated with the formation of fast-growing spinels above the chromia layer. Intergranular oxide (Al_2O_3) is microstructure dependent as it grows along grain boundaries, which results in important disparities due to grain boundaries discontinuous location. As-received alloy presents a γ' volume fraction of 40%. Aging heat treatment induces microstructural evolutions with possible impact on the mechanical properties: for γ'_{I} primary precipitates (1 to 5 μm in initial size, evolving according to an LSW law $r^3 - r_0^3 = kt$ [24]) and for γ'_{II} secondary precipitates (40 nm in initial size, diffusion-controlled growth [24]). The precipitates depletion zone was evaluated based on the primary precipitates distribution on 500-μm-thick samples. EDS line scans analyses demonstrate elements depletion thicknesses from metal/oxide interface to 99% nominal composition as summarized in Table 2. The bulk concentration of chromium in the 20-μm-thick oxidized samples is also presented since the Cr-depleted zone reaches the center of the smallest samples.

The chromium depletion ensues from supplying the chromia reaction. The precipitates provide aluminum and titanium to the external titania and internal alumina formations but also participate to the chromia reaction as a non-negligible chromium concentration can be found onto the primary precipitates [25]. The TCP-depleted layer was unexpected to overtake the Cr depletion depth as entities depletions are expected to outcome from alloys starvation. Although chromium depletion of tens of micrometers is observed for bulk specimens, thin specimens with initial thickness of 20 μm manifest bulk concentration starvation. The γ matrix reveals a Cr concentration of 18 ± 1 weight percent. A bulk concentration reduction down to 50% can be observed in the 20-μm-thick sample exposed at 800 °C for 300 h. The Cr depletion does not yet affect the chromia layer thickness nor the internal intergranular oxidation depth and primary precipitates depletion width as corroborated by Fig. 3. No external spinel was observed above the chromia layer for this condition. However,

spinel formation occurred for 900 h after 100 h with bulk chromium concentration of 1.5 weight percent. The breakaway mechanism is initiated with spinel formation yet controlled via diffusion of entities through the chromia layer leading to no apparent breakaway onto the mass gain measurements as observed by Fedorova et al. on AM1 alloy [26]. Local fast-growing spikes were observed with a maximal oxide thickness of 45 μm for 900 °C – 300 h on a 20-μm-thick sample (see Fig. 3e). As 1.5 wt% is very small in comparison with the initial content, and because there is almost no Cr concentration gradient when breakaway occurs, using the simplified approach of Eq. 1 to determine the time to breakaway is justified.

The microstructure gradient resulting from the surface reactions is expected to impact the mechanical behavior of the sample. The secondary and tertiary precipitates depletion layer, known as the hardening phase of γ/γ′ alloys, along with grain size evolution and a much wider size-reduced γ′ layer introduces an external ductile softer layer coherent with the external harder but brittle chromia layer. The impact of this microstructural gradient with regard to the thickness of the sample is to be addressed in the following mechanical results section.

Tensile Behavior of Pre-Oxidized Ultrathin Samples

Tensile tests were performed at room temperature on samples with thicknesses ranging from 20 to 500 μm with different metallurgical states, i.e., the "as-received" state, aged and oxidized states at 800 °C for 200 and 600 h. Stress–strain curves of pre-oxidized specimens during 200 h and 600 h at 800 °C are illustrated in Fig. 4. A significant thickness debit, *i.e.,* a significant drop of the strength properties and ductility due to oxidation, is evidenced. Tensile properties are significantly affected with the increase of the pre-oxidation time and the decrease in sample thickness. While samples thicker than 50 μm demonstrate significant plasticity with strain hardening, 20-μm-thick samples failed in a nearly brittle manner due to the significant portion of the oxidation-affected region.

The evolution of the macroscopic tensile properties as a function of the sample thickness for all the sample variants has been estimated from the stress–strain curves. The values of yield strength (YS), the ultimate tensile strength (UTS) and the ductility have been normalized by same proprieties obtained for thick "as-received" specimens and are compared Fig. 5. Each point in Fig. 5 represents an average of four to six mechanical tests. The normalization aims to directly evidence how aging and oxidation affect macroscopic tensile properties of the virgin material.

First, the effect of using thin specimen on the tensile test results can be evaluated on non-oxidized samples. While no evolution of the yield strength (YS) is observed for samples thicker than 100 μm, the yield strength of the as-received material dropped down for thinner samples, as illustrated in Fig. 5a. This size effect is typical of the polycrystal-to-multicrystal transition due to the presence of the free surface [10]. Similar trends are evidenced for the evolution of the ductility and the UTS as a function of the thickness, with a transition thickness of

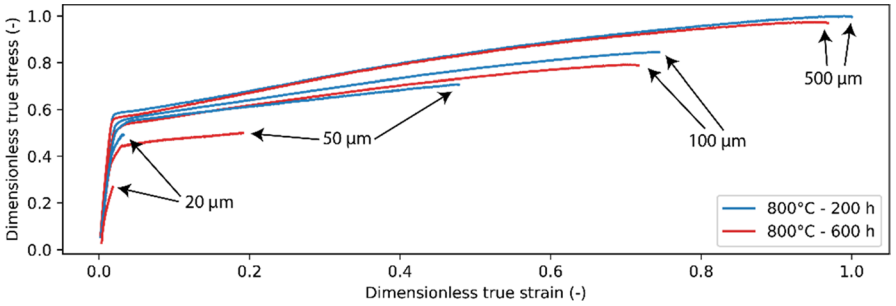

Fig. 4 True strain vs true stress for oxidized condition at 800 °C for 200 h and 600 h

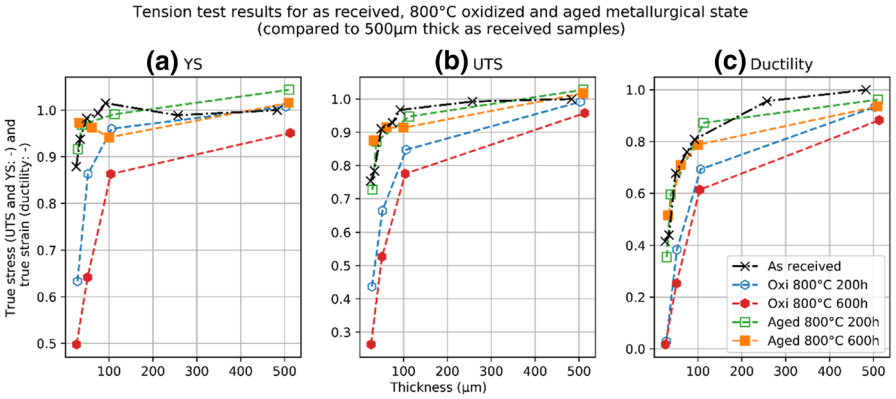

Fig. 5 Evolution of the tensile properties as a function of the sample thickness of as-received (black), 800 °C oxidized (blue 200 h, red 600 h) and aged (green 200 h, orange 600 h) metallurgical states. **a** Yield stress from true stress, **b** ultimate tensile stress from true stress and **c** ductility from true strain (Color figure online)

250 µm. YS is impacted down by 15.6%, UTS down by 32.3% and ductility down by 67.5% for 20-µm-thick samples compared to the reference polycrystalline behavior. The free-surface grains are reported not to respond similarly to core grains due to change in grain confinements. The absence of grain boundaries to pin dislocations favors dislocation escapes and subsequently delays dislocation cell and network to form, participating in strain hardening [27–29].

Second, the effect of microstructural aging alone can be studied looking at the aged specimens behavior compared to as-received specimens. Indeed, it has been verified that aged material is deprived of any oxidation-affected layer. Furthermore, the microstructural evolutions are then present in the entire volume of the sample. Aged samples at thickness 20 µm and 50 µm exhibit similar mechanical properties in terms of YS, UTS and ductility compared to the as-received material for equivalent sample thicknesses. The aged 100-µm- and 500-µm-thick samples present minor variations around the as-received state for YS and UTS but noticeable decrease in ductility. A gap appears for 100 µm and 500 µm thicknesses among the 200 h and 600 h heat treatments, with superiority to the 200 h.

The multicrystal-to-polycrystal transition is less explicit than as-received state with up to 8% variations in YS, UTS and ductility for both heat treatment times, even though a clear slope change is observed at 100 μm. The predominant differences between 200 and 600 h aged materials arise from the presence of TCP phases and γ'_{II} and γ'_{III} size evolutions. TCP appears along grain boundaries and primary precipitates in 600 h heat-treated samples. TCP particles are known to play a key role in the creep life of superalloys but reveal minor impact on their tension behavior, especially at room temperature [22, 24]. Minor microstructural evolutions are expected for the primary precipitates, resulting in minor tension behavior changes. This quantitative evaluation for the modification of mechanical properties cannot be directly linked to the quantification of the depth of the subsurface-affected zone determined in Table 2 since the oxidized samples characterized do not correspond to same oxidation treatment as samples used for the tensile tests, not yet characterized with same details. However, a discussion on tendencies is still possible.

Oxidized samples demonstrate a drop of mechanical properties compared to both as-received and aged metallurgical states. 20-μm-thick samples broke at the onset of plasticity, around 2 to 3% of the maximal true strain, with a YS and UTS significantly below the as-received and aged states. Thin samples for 200 h and 600 h oxidation exhibit lower mechanical properties in YS and UTS, with up to 36.6 and 50.2% YS decrease, and up to 56.3% and 73.7% UTS decrease for 20-μm-thick sample for oxidation times of 200 h and 600 h, respectively. Local breakaway is expected to emerge for the condition 800 °C oxidized 600 h, even so the tendency does not reveal any major breakdown compared to the 200 h oxidized samples. Mechanical properties drop from oxidation due to the brittle external chromia layer, the presence of internal alumina spikes and a ductile primary precipitates-free layer. This observation is accentuated with an increase of the oxidation-affected thickness versus total thickness ratio. External and intergranular oxidation along with the Cr- and TCP-depleted layers (as evaluated previously in Table 2 and shown in Fig. 3) demonstrates the critical role of surface reactivity onto the mechanical properties, as revealed by the drop from aged to oxidized results. The low mechanical performance of samples oxidized during 600 h compared to the ones oxidized during 200 h arises from the extension of the oxidation-affected layer increasing with the oxidation duration due to premature damage within the oxidation-affected layer. Such low results on thin sample could emanate from the damaging of grain boundaries on the entire thickness from oxidation, leading to a major drop in ductility [19].

Conclusions

The study of oxidation kinetics and its influence on the mechanical behavior of a turbine disk γ/γ' superalloy highlighted the following main conclusions:

- Isothermal oxidations in air follow parabolic regime for all temperature studied between 650 °C and 1000 °C. The oxidation kinetics are in agreement with similar type of alloys. Oxidation leads to formation of several oxides: a dense external

chromia layer, sparsely distributed titania islets and intergranular alumina regardless of the temperature and sample thickness. Spinel oxide phase is to occur for high temperature, long duration and low thickness samples, leading to local breakaway phenomenon. Size effect, i.e., volume-limited effects, has been here evidenced using ultrathin samples down to 15 μm.

- Microstructural evolution inherent to oxidation at 800 °C leads to surface and subsurface alteration with chromium-, precipitates- and TCP-depleted layers, whose respective depth had been determined on sample cross-sectional observations in order to establish the influence subsurface changes on mechanical response.
- The mechanical behavior of as-received metallurgical state using ultrathin samples evidenced a multicrystalline-to-polycrystalline transition for samples about 100 μm thick, affecting the YS, UTS and strain-to-failure.
- Samples aged for 200 h and 600 h at 800 °C show moderate evolutions of tensile properties when compared to the as-received reference state. The impact of the metallurgical evolutions among the two heat treatment times is to be observed on YS, UTS and ductility for thickness even superior to 100 μm.
- Oxidized specimens are highlighting the consequences of the microstructural gradient and subsurface embrittlement in the oxidation-affected layer. A significant drop is observed in YS, UTS and ductility for all thicknesses, especially compared to specimens without the surface/subsurface-affected layers. The thickness of the gradient of microstructure, larger for 600 h than for 200 h heat treatment, can be witnessed with the lower mechanical performances of samples oxidized during 600 h.

Acknowledgements The authors would like to acknowledge Karim Choquet (ICA) and Remi Roumiguier (MIDIVAL) for technical help. This study was supported by SAFRAN Tech, SAFRAN Aircraft Engine and the Agence Nationale de la Recherche (ANR) [ANR-18-CE08-0003; ANR-JCJC-COMPAACT project funded from the AAPG2018].

References

1. S. Bose, *High temperature coatings*, (Elsevier, Butterworth-Heinemann, 2018).
2. Young DJ. *High Temperature Oxidation and Corrosion of Metals Second Edition*. Elsevier; 2016.
3. J. Tong, S. Dalby, J. Byrne, M. B. Henderson, and M. C. Hardy, Creep, fatigue and oxidation in crack growth in advanced nickel base superalloys. *International Journal of Fatigue.* **23**, 2001 (897–902).
4. A. Pineau and S. D. Antolovich, High temperature fatigue of nickel-base superalloys – A review with special emphasis on deformation modes and oxidation. *Engineering Failure Analysis.* **16**, 2009 (2668–2697).
5. H. E. Evans, A. T. Donaldson, and T. C. Gilmour, Mechanisms of Breakaway Oxidation and Application to a Chromia-Forming Steel. *Oxidation of Metals.* **52**, 1999 (379–402).
6. M. Zupan, M. J. Hayden, C. J. Boehlert, and K. J. Hemker, Development of high-temperature microsample testing. *Experiment mechanics.* **41**, 2001 (242–247).
7. Texier D, Castro Moreno A, Monceau D, Hourcade D, Velay V, Andrieu E. Size effect on the plastic behaviour of polycrystalline materials: grain size, free surface and precipitation state. *Submitted in Acta Materialia*. .

8. Texier D, Ecochard M, Gheno T, Lours P. Screening breakaway in MCrAlY coatings for short-term oxidation at high temperature. *Submitted in Corrosion Science*. .
9. D. J. Young, A. Chyrkin, and W. J. Quadakkers, A Simple Expression for Predicting the Oxidation Limited Life of Thin Components Manufactured from FCC High Temperature Alloys. *Oxid Met.* **77**, 2012 (253–264).
10. C. Keller, E. Hug, and X. Feaugas, Microstructural size effects on mechanical properties of high purity nickel. *International Journal of Plasticity.* **27**, 2011 (635–654).
11. D. Texier, D. Monceau, J. C. Salabura, R. Mainguy, and E. Andrieu, Micromechanical testing of ultrathin layered material specimens at elevated temperature. *Materials at High Temperatures.* **33**, 2016 (325–337).
12. Bradski G. The OpenCV library. *Dr. Dobb's Journal of Software Tools*. 2000;
13. Sutton MA, Orteu JJ, Schreier H. *Image Correlation for Shape, Motion and Deformation Measurements: Basic Concepts,Theory and Applications*. Springer Science & Business Media; 2009.
14. C. Wagner, Beitrag zur Theorie des Anlaufvorgangs. *Zeitschrift für Physikalische Chemie.* **21B**, 1933 (25–41).
15. R. Malacarne, L. Aranda, S. Mathieu, C. Desgranges, S. Knittel, M. Vilasi. Long-term isothermal oxidation behavior of two industrial polycrystalline nickel base alloys at 700°C – Evaluation of intergranular oxidation distribution and kinetic. *submitted same Issue*. 2020;
16. J. H. Chen, P. M. Rogers, and J. A. Little, Oxidation behavior of several chromia-forming commercial nickel-base superalloys. *Oxid Met.* **47**, 1997 (381–410).
17. E. Chateau and L. Rémy, Oxidation-assisted creep damage in a wrought nickel-based superalloy: Experiments and modelling. *Materials Science and Engineering: A*. **527**, 2010 (1655–1664).
18. Thébaud L. Etude des relations entre microstructure et propriétés mécaniques du nouveau superalliage base nickel AD730^{TM}. PhD Thesis, ISAE-ENSMA; 2017.
19. A. A. N. Németh, D. J. Crudden, D. E. J. Armstrong, et al., Environmentally-assisted grain boundary attack as a mechanism of embrittlement in a nickel-based superalloy. *Acta Materialia.* **126**, 2017 (361–371).
20. Wessman A, Laurence A, Cormier J, Villechaise P, Billot T, Franchet J-M. Thermal Stability of Cast and Wrought Alloy Rene 65. In: *Superalloys 2016*. Hoboken, NJ, USA: John Wiley & Sons, Inc.; 2016:793–800. doi:https://doi.org/10.1002/9781119075646.ch85.
21. Laurence A, Cormier J, Villechaise P, et al. Impact of the Solution Cooling Rate and of Thermal Aging on the Creep Properties of the New Cast & Wrought René 65 Ni-Based Superalloy. *8th International Symposium on Superalloy 718 and Derivatives*. 2014;333–348. doi:10/ggf72s.
22. Laurence A. Impact du sur-vieillissement métallurgique sur le comportement et la durabilité du nouveau superalliage pour disque de turbine René 65. PhD Thesis, ISAE-ENSMA; 2015.
23. R. L. Amaro, S. D. Antolovich, R. W. Neu, and P. M. Singh, High temperature oxidation and γ depletion in the single-crystal superalloy PWA 1484. *Materials at High Temperatures.* **33**, 2016 (476–488).
24. Wessman A. Physical Metallurgy of Rene 65, a Next-Generation Cast and Wrought Nickel Superalloy for use in Aero Engine Components. PhD Thesis, University of Cincinnati; 2016.
25. A. R. P. Singh, S. Nag, S. Chattopadhyay, et al., Mechanisms related to different generations of γ' precipitation during continuous cooling of a nickel base superalloy. *Acta Materialia.* **61**, 2013 (280–293).
26. E. Fedorova, D. Monceau, and D. Oquab, Quantification of growth kinetics and adherence of oxide scales formed on Ni-based superalloys at high temperature. *Corrosion Science.* **52**, 2010 (3932–3942).
27. C. Keller, E. Hug, R. Retoux, and X. Feaugas, TEM study of dislocation patterns in near-surface and core regions of deformed nickel polycrystals with few grains across the cross section. *Mechanics of Materials.* **42**, 2010 (44–54).
28. Mughrabi H. Some consequences of surface and size effects in plastically deformed copper single crystals. *physica status solidi (b)*. 1971;44:391–402.
29. J. T. Fourie, Sub-surface dislocation structure of deformed copper. *The Philosophical Magazine: A Journal of Theoretical Experimental and Applied Physics.* **21**, 1970 (977–985).

Authors and Affiliations

Charles Romain[1] · Damien Texier[1] · Clara Desgranges[2] · Jonathan Cormier[3] · Stéphane Knittel[4] · Daniel Monceau[5] · Denis Delagnes[1]

Damien Texier
damien.texier@mines-albi.fr

[1] Institut Clément Ader (ICA) - UMR CNRS 5312, Université de Toulouse, CNRS, INSA, UPS, Mines Albi, ISAE-SUPAERO, Campus Jarlard, Albi, France

[2] Materials and Processes Department, SAFRAN-Tech, Rue des Jeunes Bois, Châteaufort, Magny-les-Hameaux, France

[3] Institut Pprime, UPR CNRS 3346, ISAE-ENSMA, Chasseneuil-du-Poitou, France

[4] SAFRAN Aircraft Engines, Evry, France

[5] CIRIMAT, Université de Toulouse, CNRS, INPT, UPS, ENSIACET, Toulouse, France